PROCEEDINGS OF SPIE

SPIEDigitalLibrary.org/conference-proceedings-of-spie

Developing a low-cost multispectral imager for detecting algal blooms in rivers

Shannon Hamp, Riley Logan, Joseph Shaw

Shannon M. Hamp, Riley D. Logan, Joseph A. Shaw, "Developing a low-cost multispectral imager for detecting algal blooms in rivers," Proc. SPIE 12327, SPIE Future Sensing Technologies 2023, 123270J (22 May 2023); doi: 10.1117/12.2645373



Event: SPIE Future Sensing Technologies, 2023, Yokohama, Japan

Developing a low-cost multispectral imager for detecting algal blooms in rivers

Shannon M. Hamp^a, Riley D. Logan^a, and Joseph A. Shaw^{a, b}

^aElectrical and Computer Engineering Department, Montana State University, P.O. Box 173780, Bozeman, Montana 59717-3515 USA

^bOptical Technology Center, P.O. Box 173515

ABSTRACT

A low-cost multispectral imager is described for routine monitoring of Cladophora nuisance algae and blue-green algae in narrow rivers that are not spatially resolved by satellites. The goal is to identify algal blooms and estimate the chlorophyll a (chl a) and phycocyanin content from a network of low-cost imagers that can be mounted on bridges, trees, or other convenient objects at key river locations. The preliminary design uses Raspberry Pi cameras and computers with bandpass filters at 568, 671, 700, and 825 nm, based on data gathered with an airborne hyperspectral imager on the Upper Clark Fork River in southwestern Montana USA. This paper summarizes the initial design, calibration measurements, and preliminary reflectance data.

Keywords: River remote sensing, multispectral imaging, algae, water quality, Cladophora

1. INTRODUCTION

The prevalence of filamentous green algae in a riparian ecosystem threatens the health of the ecosystem's flora and fauna. Filamentous algal blooms add to the accumulation of benthic organic matter and ultimately contribute to the depletion of dissolved oxygen in the affected waterway. While filamentous algal blooms disrupt benthic conditions and contribute to oxygen depletion, the blooms also indicate damaging nutrient enrichment and can be directly related to water quality through metrics such as chl a concentration. This motivates the quantification of algal blooms for indirect measurement of water quality in support of healthier riparian ecosystems. This paper focuses specifically on the growth of Cladophora glomerata algae that frequently produces nuisance blooms in the Upper Clark Fork River (UCFR) in the State of Montana due to naturally high phosphorous levels and the introduction of wastewater that have led to harmful nutrient enrichment. Quantification of algal growth is especially relevant in states like Montana that have removed numeric nutrient standards for water quality in favor of indirect measurement methods such as organic matter and algae growth.

This quantification of benthic organic matter and algal blooms has been accomplished through *in-situ* spot sampling of select stretches of the Upper Clark Fork River.^{6,7,9-11} Algal growth depends on many factors including nutrient availability, water temperature, streamflow, and solar irradiance.^{3,12-16} This wide variety of influencing factors minimizes the predictability of algal growth, necessitating frequent monitoring of large areas. *In-situ* spot sampling methods are spatially limited, minimizing the ability to capture location-specific changes in the algae growth. Hyperspectral imaging from an unmanned aerial vehicle (UAV) is effective for narrow rivers that are not spatially resolved by satellites and have lower cost than conventional aircraft. UAV-based hyperspectral imaging is therefore desirable for efficiently detecting river algae over large areas with high spatial resolution.¹⁷⁻²⁶ While this measurement method provides a promising alternative to spot sampling, hyperspectral imaging systems are associated with high data density and cost. Additionally, the requirement of drone flights to collect imagery incurs additional financial risk and is largely weather dependent. These factors limit the use of hyperspectral imaging for consistent, long-term algae monitoring.

Multispectral imagers provide a low-cost alternative with lower data density than hyperspectral imagers that enables long-term algae monitoring. These benefits of multispectral imaging are due to the reduction of

Further author information: (Send correspondence to Joseph A. Shaw) E-mail: joseph.shaw@montana.edu, Telephone: 1 406 994 7261

SPIE Future Sensing Technologies 2023, edited by Osamu Matoba, Joseph A. Shaw, Christopher R. Valenta, Proc. of SPIE Vol. 12327, 123270J ⋅ © 2023 SPIE 0277-786X ⋅ doi: 10.1117/12.2645373

wavelength bands in a multispectral system to include several salient channels, rather than the nearly continuous spectrum that is characteristic of a hyperspectral imager. While multispectral imagers do not capture the full spectrum, they have been found to be useful in algae monitoring applications.^{27–41} With a sufficiently low-cost and robust design, several multispectral imagers could be deployed on bridges, trees, posts, etc. along a river stretch to provide long-term information about the algal growth in the river. Our aim is to develop a viable, long-term monitoring system for narrow rivers that cannot be resolved on satellites using a network of remotely operating, low-cost multispectral imagers that are supplemented with a UAV-based hyperspectral imager when conditions are detected that warrant further investigation.

In this paper, we build on our recent work using drone-based hyperspectral imagery for remote sensing of river algae by applying the salient wavelengths selected using our hyperspectral imaging system to develop a deployable, low-cost multispectral imager. Specifically, we present the development and testing of this low-cost multispectral imager for continuous, long-term monitoring of *Cladophora* nuisance algae in shallow, clear, cobble-bed rivers.

2. METHODS

This section describes the development and experimental testing of the proof-of-concept, low-cost multispectral imager. This discussion is introduced with the construction process of the imaging system, followed by imager characterization and calibration methods, the experimental setup for field testing, and final analysis of the resulting field data.

2.1 Imager Design and Construction

The multispectral imaging system was designed to monitor *Cladophora* algae by imaging at wavelengths that are indicative of this algae species, but with a lower cost and data density than the hyperspectral imaging system. Four spectral bands were selected as strong indicators of *Cladophora*. The first band was a yellow-green band located at 568 nm owing to the visible green color of *Cladophora*. Two red bands were also implemented at 671 and 700 nm based on common band ratios found in algae sensing literature. ^{17,18,42} A final near-infrared (NIR) band was selected at 825 nm to aid in the distinction between bank vegetation and submerged algae that typically has a weakened NIR response due to water absorption. ⁴³ These band selections were also informed by hyperspectral imagery of *Cladophora* in the Upper Clark Fork River using our drone-based hyperspectral imaging system on the Upper Clark Fork River for river algae pigment estimation was presented elsewhere. ⁴⁴ Each spectral band was implemented in the multispectral imager design with a physical bandpass filter that can be easily replaced if different wavelengths are determined to be useful (Table 1).

Table 1: Specifications:		

Specified CWL (nm)	Measured CWL (nm)	Measured FWHM (nm)
568.00 ± 2.0	565.5 ± 2	11 ± 2
671.00 ± 2.0	668.5 ± 2	11 ± 2
700.00 ± 2.0	699.0 ± 2	10 ± 2
825.00 ± 3.0	822.5 ± 2	27 ± 2

Each bandpass filter was placed over one of four separate Raspberry Pi V2 NoIR cameras, where the NoIR specification indicates that the cameras do not have an infrared-blocking filter, extending the spectral response of the cameras to 400 - 1000 nm. These low-cost cameras use a Sony IMX219 8 megapixel CMOS sensor and interface directly with the Raspberry Pi embedded computers. Each spectral band of the imaging system was implemented with a separate Raspberry Pi camera controlled with its own embedded computer. Specifically, three of the four cameras received direct control from peripheral Raspberry Pi Zero Ws, and the final camera received control from the master Raspberry Pi 4B that provided ultimate control of the imaging system. The Raspberry Pi 4B was selected as the master controller of the system owing to its high processing power, while the remaining cameras were controlled with Raspberry Pi Zero Ws because they have lower power requirements. The three peripheral Raspberry Pi Zero W devices were converted to "gadget mode" through software such that

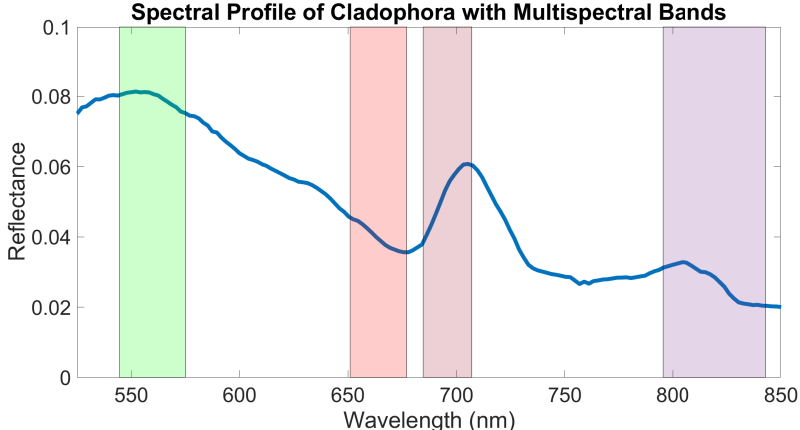


Figure 1: Spectral profile of *Cladophora* from the drone-based hyperspectral system, where the color bars indicate the wavelength bands achieved with the bandpass filters implemented in the low-cost multispectral imager.

the master Raspberry Pi 4B could communicate to the peripheral devices through USB ethernet connections. These Raspberry Pi devices and their corresponding cameras were integrated with power hardware such that the system could be enclosed in a waterproof box to enable field verification measurements (Figure 2).

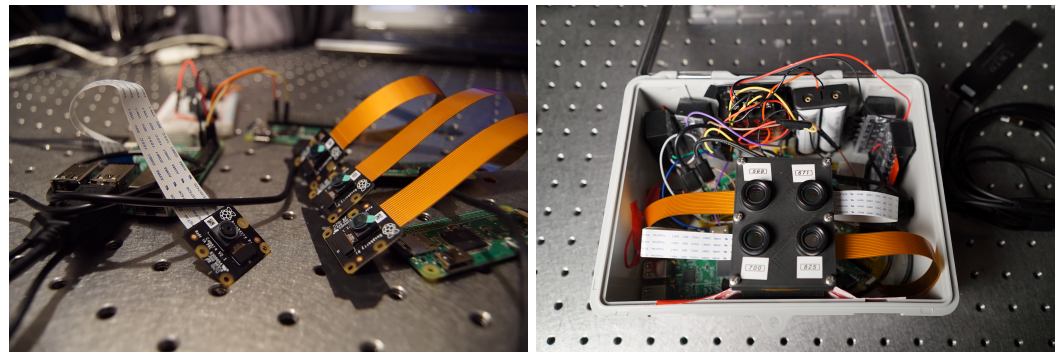


Figure 2: Low-cost multispectral algae imager prototype including the internal Raspberry Pi components (left) and the system in the enclosure (right).

2.2 Filter Transmission Characterization

The bandpass filters of Table 1 were specified to transmit light within the intended spectral bands of the imaging system, but reliable operation of the system required verification of the filter transmission across the spectral range of the Raspberry Pi cameras. This transmission verification was completed for the four filters using an integrating sphere (Labsphere model V3ND-NNNN-NNSL-NS00-0000 with 30 cm inner diameter and 10 cm aperture) and VIS-NIR spectrometer (Ocean Optics). For these measurements, each 12.5 mm filter was placed in a 12.5 mm lens tube (10.4 mm length), and mounted directly between the integrating sphere aperture and the bare-fiber spectrometer probe. For each filter, the spectral transmittance was acquired as a ratio of the intensity measured through the filter, divided by a direct reference measurement of the integrating sphere output, without the filter in the optical setup:

$$Spectral\ Transmittance = \frac{DN_{filter}}{DN_{reference}}.$$
 (1)

The filters were examined from 400 to 1000 nm and no significant leakage wavelengths were found. The resulting normalized measurements were then smoothed with a moving mean function, where each average value was calculated over a sliding window that encompassed seven values at a time (Figure 3). These transmittance

measurements were used to compute the center wavelength (CWL) and the full width half maximum (FWHM) values corresponding to each bandpass filter (Table 1).

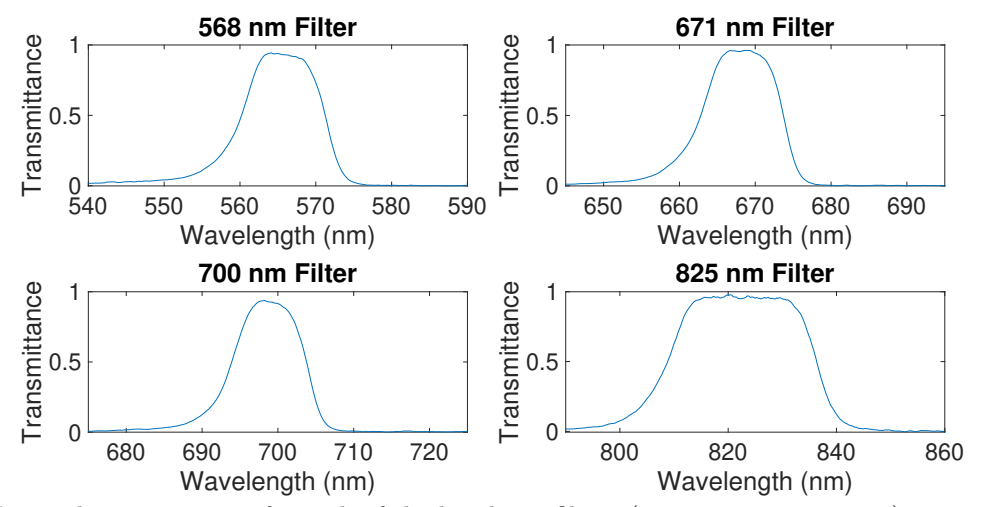


Figure 3: Spectral transmittance for each of the bandpass filters (568, 671, 700, 825 nm) as measured using the integrating sphere output and spectrometer. Data were normalized to a direct reference measurement of the integrating sphere output.

2.3 Relative Spectral Response Characterization

The spectral response was characterized for each of the four Raspberry Pi V2 NoIR camera modules to evaluate the response of the camera as a function of wavelength, and to confirm that the camera modules performed similarly to one another for use in the multispectral imager design.

The spectral response measurements were completed for each camera with the Raspberry Pi board that it would be controlled with in the multispectral imager design (one with the master Raspberry Pi 4B, and the others with the three peripheral Raspberry Pi Zero Ws). The optical setup for the spectral response measurements used a grating monochromator (Acton Research Monochromator SpectraPro-150). A blue-blocking filter was also included at the output slit of the monochromator for measurements beyond 700 nm to minimize the effects of the second-order diffraction spots that are present in the monochromator output. The spectral transmittance of this filter was also characterized with the integrating sphere and spectrometer probe using the same process that was described for the measured bandpass filters. These measurements confirmed that the transmission of the blue-blocking filter was < 1% at wavelengths below 600 nm and > 90% at wavelengths greater than 650 nm. Each camera was placed in front of the exit slit of the monochromator, allowing the output of the monochromator to be imaged as the monochromator output was swept through the specified spectral range of the cameras (400 - 1000 nm) in 10 nm steps.

The gain, or "ISO" setting as defined in the Raspberry Pi documentation, was held at a value of 1 for all measurements; however, the exposure time, or "Shutter Speed", setting of the cameras was governed by the output power of the monochromator. Since the output power of the monochromator varied with wavelength, ⁴⁵ the exposure time required adjustment across the wide spectral range to maintain ample signal. This variation in the exposure time of the images was accounted for by relying on the linear relationship that has been shown to exist⁴⁶ between the exposure time and signal such that a pixel multiplier could be applied to each image based on the exposure time.

The spectral response measurements for each camera were then normalized to the output power of the monochromator by dividing each image by the direct reference measurements taken using the optical power meter. Then, the spectral response measurements were separated into the red, green, and blue channels and normalized to the maximum digital number of each corresponding channel, producing a relative spectral response in the red, green, and blue channels for each of the four cameras. The relative spectral response of the four cameras

were then averaged to produce Figure 4. The standard deviation between the four cameras was then computed for each channel at each wavelength to determine how similarly the camera modules performed to one another for use in the multispectral imager. These standard deviation values were averaged within the spectral bounds of each bandpass filter and included in Figure 4 as errorbars confined to the spectral region of the bandpass filters that are represented by the color bars. Reflectance calibrations for the 568 nm band were completed using the green channel, which exhibited an average standard deviation of 0.0125 in that band. Reflectance calibrations for the 671 nm, 700 nm, and 825 nm were completed using the red band, which exhibited average standard deviations of 0.0106, 0.0103, and 0.0489, respectively.

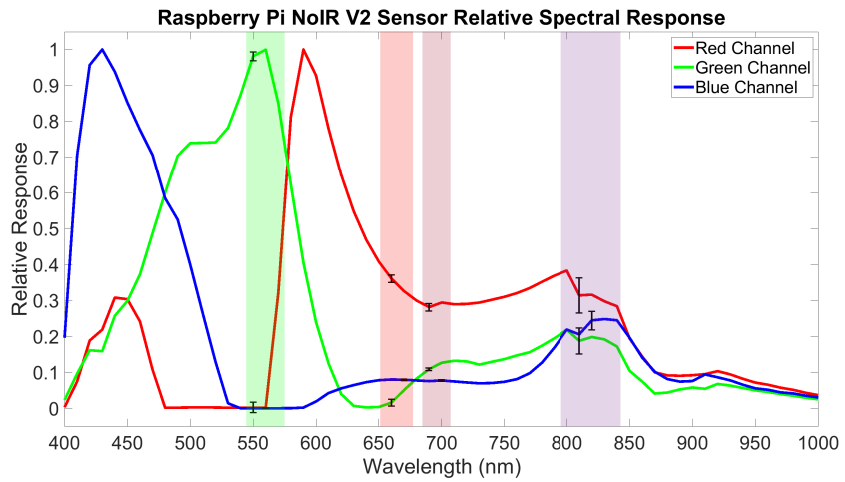


Figure 4: Relative spectral response, presented as the average of the measurements completed for four separate Raspberry Pi NoIR v2 cameras. The error bars represent the average standard deviation within the spectral limits of the bandpass filters that are represented by the color bands.

Despite the adjustment of imager exposure time to align with the output power of the monochromator, the spectral channels exhibit regions where their response is zero. This does not align with the relative spectral response measurements for the Raspberry Pi V2 camera conducted by Pagnutti et al.⁴⁶ These regions of no signal align with wavelengths of low monochromator output power. Therefore, the exposure time was most likely not adjusted enough to account for this variation in signal. These regions of zero signal were not further evaluated because they do not overlap with the spectral bands selected for the multispectral imager.

2.4 Flat Field Calibration

In addition to verifying the spectral response of the imager, it was also necessary to compensate for pixel-to-pixel response variations. This compensation was required to convert an entire image capture in the field to reflectance with only a small group of pixels viewing a reflectance target. These calibration measurements were collected by directly imaging the output of an integrating sphere (Labsphere model V3ND-NNNN-NNSL-NS00-0000 with 30 cm inner diameter and 10 cm aperture) with each camera.

Using this optical setup, fifty images of the integrating sphere aperture were captured with each camera, where the imaging area of the aperture was procedurally shifted after every ten images to minimize the effect of scene nonuniformities. As in the relative spectral response measurements discussed in Section 2.3, the calibration measurements for each camera were captured with the Raspberry Pi board with which each camera would be controlled. The fifty images captured with each camera were then used to develop pixel-multiplier matrices for each camera to achieve a uniform pixel-to-pixel response. This was accomplished by first averaging the fifty images, and then normalizing the red, green, and blue channels to the mean value within each channel. This produced a flat field calibration matrix for each camera to be applied to river data to minimize pixel-to-pixel variation in the calibrated imagery.

The required magnitude of pixel correction was quantified with normalized standard deviation values for each color channel. From the average of the 50 images, the standard deviation was computed for each camera

across each red, green, and blue channel. The standard deviations corresponding to each channel were then averaged across the four cameras and normalized to the average mean of each channel. The resulting magnitude of correction was 1.38% for the red channel, 4.07% for the green channel, and 3.78% for the blue channel.

2.5 Field Verification

Following laboratory calibrations, the performance of the low-cost multispectral imager was assessed at the Deer Lodge field site along the Upper Clark Fork River (46.378543, -112.737119) on 9 August 2022 and again on 15 September 2022.

2.5.1 Optical Setup

From the bank of the river, multispectral and hyperspectral data were collected for direct comparison of reflectance values between the two imaging systems. The hyperspectral imager utilized in this experimental setup was the Resonon Pika L imager with a spectral range of 400 - 1000 nm and a spectral resolution of 2.1 nm.

Imagery was captured by both imagers at the same time to minimize discrepancies in light conditions (sun angle, clouds, etc.) between the two data sets. For each field campaign, the optical setup utilized a reflectance target for image calibration as well as five hoops indicating areas of spatial homogeneity on the river bottom for comparison between the hyperspectral and multispectral data (Figure 5).

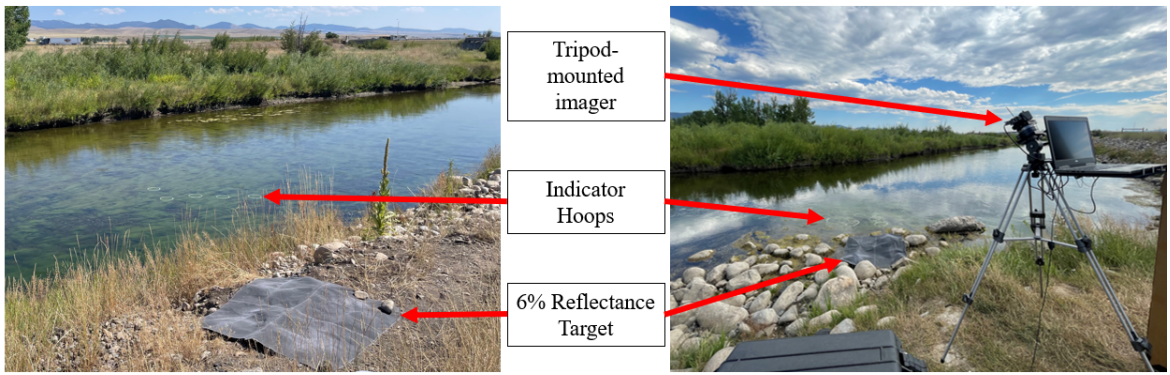


Figure 5: Optical setup for field verification of the multispectral imager.

2.5.2 Image Processing

Inclusion of the reflectance target in the images allowed for correction to reflectance for direct comparison between the two imaging systems. For the multispectral imager, this correction first required application of the flat-field correction matrices discussed in Section 2.4 to compensate for pixel-to-pixel response variations. The flat-field images were then corrected to reflectance, where reflectance is a ratio of incident light to reflected light. This reflectance correction was completed by averaging the digital number response of the pixels associated with the reflectance target such that the entire image could be corrected by dividing each pixel by the average target digital number and multiplying by its known reflectance of 6%. This produced an image where each pixel value no longer had a digital number value from 0 to 255, but instead had a reflectance value from 0 to 1, where 1 indicates 100% reflection. Corresponding hyperspectral data were collected using the same optical setup as the multispectral imager and corrected with the reflectance target in the same manner as the multispectral data, where the image was normalized to the average reflectance target digital number and multiplied by the known reflectance value.

The multispectral imager performance was evaluated utilizing field data collected on the Upper Clark Fork River throughout the 2022 algae season. These data were analyzed with respect to the hyperspectral imager by performing a percent error calculation for each set of reflectance values using the following equation:

$$Percent \ Difference = \frac{Reflectance_{multispectral} - Reflectance_{Hyperspectral}}{Reflectance_{Hyperspectral}}. \tag{2}$$

The resulting percent error values were averaged for each spectral band to produce a single value for each wavelength band.

3. RESULTS AND DISCUSSION

In this section, we discuss the results of the field verification measurements obtained for the multispectral imager along the Upper Clark Fork River. This was accomplished by directly comparing the reflectance values calculated from multispectral data to the reflectance values calculated from hyperspectral data within the spatial bounds of the indicator hoops placed in the river.

The direct comparison between the multispectral and hyperspectral imaging systems demonstrated that the proof-of-concept imager produced reflectance values within approximately 13% of the hyperspectral imagery in a field setting, where the 825 nm channel demonstrated the lowest percent error (11.90%) and the 700 nm channel demonstrated the highest percent error (15.44%) (Table 2). These field verification measurements were completed with a degraded reflectance target that could have increased the percent difference values. Future comparisons between the two imaging systems with downwelling irradiance sensors, as opposed to reflectance targets, are likely to improve the agreement between the multispectral and hyperspectral data sets.

Table 2: Direct percent differences between the multispectral and hyperspectral imaging systems with respect to each of the four multispectral channels in the multispectral imager. The data set is comprised of ten data points, where each indicator hoop produces a data point.

Wavelength Channel (nm)	Percent Difference (%)
568.00	12.03
671.00	12.30
700.00	15.44
825.00	11.90

The Resonon Pika L hyperspectral imager that was used in this optical setup is the same imager that we fly on a UAV to collect algae imagery. Our initial hyperspectral algorithms for estimating chl a and phycocyanin content from this imaging system use band ratios in which systematic errors tend to cancel.⁴⁴ In the future, these band ratios will be used with the multispectral imaging system as well to estimate chl a and phycocyanin content while minimizing systematic errors.

4. CONCLUSION

In this paper, we presented the design, calibration, and assessment of an initial proof-of-concept multispectral imaging system for detecting *Cladophora* algae in the Upper Clark Fork River. This river is a shallow, clear, cobble-bed river that experiences large *Cladophora* algae blooms resulting from naturally high phosphorous levels and the introduction of wastewater that have led to harmful nutrient enrichment. The development of this low-cost multispectral imager was motivated by the growing need for indirect water quality assessment through metrics such as algae growth.

The multispectral imager was constructed with Raspberry Pi components to maintain low cost. The four wavelength bands of the imager were informed by salient wavelengths identified with our drone-based hyperspectral imaging system and implemented as physical bandpass filters in the system. Following the calibration of the imaging system, field imagery was collected alongside a tripod-mounted hyperspectral imager for direct comparison between the reflectance values produced by the two imaging systems. This comparison demonstrated that the low-cost multispectral imager produced reflectance values within 11.9 to 15.4% of the hyperspectral system.

The prototype multispectral imager for algae detection presented in this paper demonstrates progress toward a low-cost, commercializable imaging system for water quality applications. Currently, a second prototype is being developed with four monochrome sensors to reduce measurement uncertainty and unnecessary data density resulting from the RGB sensors. This new prototype design has lower power requirements to improve upon power limitations for long-term algae monitoring in the field. The second prototype will also mitigate the need for active user operation such that the system will support stand-alone operation for two-week periods of time. In future

work, additional efforts will also be made to extend the application of the imaging system to additional field sites along Montana rivers including the Upper Clark Fork and the Gallatin River. Finally, future verification of the system will include the collection of ground-truthing data to determine the accuracy with which the low-cost multispectral imager estimates chlorophyll A and phycocyanin concentration.

ACKNOWLEDGMENTS

This work was funded, in part, by the NSF EPSCoR Consortium for Research on Environmental Water Systems Cooperative Agreement OIA-1757351. This work was also funded by the NSF Research Experience for Undergraduates Program, as well as the Undergraduate Scholars Program at Montana State University.

REFERENCES

- [1] Stevenson, R., Bennett, B., Jordan, D., and French, R., "Phosphorus regulates stream injury by filamentous green algae, do, and ph with thresholds in responses," *Hydrobiologia* **695** (2012).
- [2] Peipoch, M. and Valett, M. H., "Trophic interactions among algal blooms, macroinvertebrates, and brown trout: Implications for trout recovery in a restored river," *River Research and Applications* **35**(9), 1563–1574 (2019).
- [3] Dodds, W. K., "Factors associated with dominance of the filamentous green alga cladophora glomerata," Water Research 25(11), 1325–1332 (1991).
- [4] Chételat, J., Pick, F. R., Morin, A., and Hamilton, P. B., "Periphyton biomass and community composition in rivers of different nutrient status," *Canadian Journal of Fisheries and Aquatic Sciences* **56**(4), 560–569 (1999).
- [5] Biggs, B. J. F., "Eutrophication of streams and rivers: dissolved nutrient-chlorophyll relationships for benthic algae," *Journal of the North American Benthological Society* **19**(1), 17–31 (2000).
- [6] Dodds, W., Smith, V., and Zander, B., "Developing nutrient targets to control benthic chlorophyll levels in streams: A case study of the clark fork river," Water Research 31(7), 1738–1750 (1997).
- [7] Suplee, M., Watson, V., Dodds, W., and Shirley, C., "Response of algal biomass to large-scale nutrient controls in the clark fork river, montana, united states," JAWRA Journal of the American Water Resources Association 48 (2012).
- [8] "Repeal numeric nutrient standards for water quality, sb 358, 67th legislature," (2021).
- [9] Lohman, K. and Priscu, J. C., "Physiological indicators of nutrient deficiency in cladophora (chlorophyta) in the clark fork of the columbia river, montana," *Journal of Phycology* **28**(4), 443–448 (1992).
- [10] Parker, S. R., Gammons, C. H., Poulson, S. R., and DeGrandpre, M. D., "Diel variations in stream chemistry and isotopic composition of dissolved inorganic carbon, upper clark fork river, montana, usa," *Applied Geochemistry* 22(7), 1329–1343 (2007).
- [11] Flynn, K. F., "Methods and mathematical approaches for modeling cladophora glomerata and river periphyton," (2012).
- [12] Dodds, W. K. and Gudder, D. A., "The ecology of cladophora," Journal of Phycology 28(4), 415–427 (1992).
- [13] Wong, S. L. and Clark, B., "Field determination of the critical nutrient concentrations for cladophora in streams," *Journal of the Fisheries Research Board of Canada* **33**(1), 85–92 (1976).
- [14] Pitcairn, C. E. and Hawkes, H., "The role of phosphorus in the growth of cladophora," in [*Phosphorus in Fresh Water and the Marine Environment*], Jenkins, S. and Ives, K., eds., 159–171, Pergamon (1973).
- [15] Hill, W. R. and Boston, H. L., "Community development alters photosynthesis-irradiance relations in stream periphyton," *Limnology and Oceanography* **36**(7), 1375–1389 (1991).
- [16] Finlay, J. C., Hood, J. M., Limm, M. P., Power, M. E., Schade, J. D., and Welter, J. R., "Light-mediated thresholds in stream-water nutrient composition in a river network," *Ecology* **92**(1), 140–150 (2011).
- [17] Mishra, S., Mishra, D. R., and Schluchter, W. M., "A novel algorithm for predicting phycocyanin concentrations in cyanobacteria: A proximal hyperspectral remote sensing approach," *Remote Sensing* 1(4), 758–775 (2009).

- [18] Huang, Y., Jiang, D., Zhuang, D., and Fu, J., "Evaluation of hyperspectral indices for chlorophyll-a concentration estimation in tangxun lake (wuhan, china)," *International Journal of Environmental Research and Public Health* 7(6), 2437–2451 (2010).
- [19] Richardson, L. L., "Remote sensing of algal bloom dynamics," BioScience 46(7), 492–501 (1996).
- [20] Mehrubeoglu, M., Teng, M. Y., Savage, M., Rafalski, A., and Zimba, P. V., "Hyperspectral imaging and analysis of mixed algae species in liquid media," in [2012 IEEE International Conference on Imaging Systems and Techniques Proceedings], 421–424 (2012).
- [21] Casal, G., Sánchez-Carnero, N., Domínguez-Gómez, J. A., Kutser, T., and Freire, J., "Assessment of ahs (airborne hyperspectral scanner) sensor to map macroalgal communities on the ría de vigo and ría de aldán coast (nw spain)," *Marine Biology* **159**, 1997–2013 (2012).
- [22] Volent, Z., Johnsen, G., and Sigernes, F., "Microscopic hyperspectral imaging used as a bio-optical taxonomic tool for micro- and macroalgae," *Applied optics* 48, 4170–4176 (2009).
- [23] Craig, S. E., Lohrenz, S. E., Lee, Z., Mahoney, K. L., Kirkpatrick, G. J., Schofield, O. M., and Steward, R. G., "Use of hyperspectral remote sensing reflectance for detection and assessment of the harmful alga, karenia brevis," Appl. Opt. 45(21), 5414–5425 (2006).
- [24] Szekielda, K., Marmorino, G., Maness, S., Donato, T., Bowles, J., Miller, W., and Rhea, W., "Airborne hyperspectral imaging of cyanobacteria accumulations in the potomac river," *Journal of Applied Remote Sensing* 1, 1–14 (2007).
- [25] Page, B. P., Kumar, A., and Mishra, D. R., "A novel cross-satellite based assessment of the spatio-temporal development of a cyanobacterial harmful algal bloom," *International Journal of Applied Earth Observation and Geoinformation* **66**, 69–81 (2018).
- [26] Mishra, S. and Mishra, D. R., "Normalized difference chlorophyll index: A novel model for remote estimation of chlorophyll-a concentration in turbid productive waters," Remote Sensing of Environment 117, 394–406 (2012).
- [27] Kutser, T., Vahtmäe, E., and Martin, G., "Assessing suitability of multispectral satellites for mapping benthic macroalgal cover in turbid coastal waters by means of model simulations," *Estuarine, Coastal and Shelf Science* **67**(3), 521–529 (2006).
- [28] Hochberg, E. J. and Atkinson, M. J., "Capabilities of remote sensors to classify coral, algae, and sand as pure and mixed spectra," *Remote Sensing of Environment* 85(2), 174–189 (2003).
- [29] Cao, M., Qing, S., Jin, E., Hao, Y., and Zhao, W., "A spectral index for the detection of algal blooms using sentinel-2 multispectral instrument (msi) imagery: a case study of hulun lake, china," *International Journal of Remote Sensing* 42(12), 4514–4535 (2021).
- [30] Isenstein, E. M., Trescott, A., and Park, M.-H., "Multispectral remote sensing of harmful algal blooms in lake champlain, usa," Water Environment Research 86(12), 2271–2278 (2014).
- [31] Zibordi, G., Parmiggiani, F., and Alberotanza, L., "Application of aircraft multispectral scanner data to algae mapping over the venice lagoon," *Remote Sensing of Environment* **34**(1), 49–54 (1990).
- [32] Tóth, V. Z., Grósz, J., Ladányi, M., and Jung, A., "A new lake algae detection method supported by a drone-based multispectral camera," *Lakes & Reservoirs: Science, Policy and Management for Sustainable Use* **26**(3), e12377 (2021).
- [33] Che, S., Du, G., Wang, N., He, K., Mo, Z., Sun, B., Chen, Y., Cao, Y., Wang, J., and Mao, Y., "Biomass estimation of cultivated red algae pyropia using unmanned aerial platform based multispectral imaging," *Plant Methods* 17 (2021).
- [34] Goldberg, S., Kirby, J., and Licht, S., "Applications of aerial multi-spectral imagery for algal bloom monitoring in rhode island," (2016).
- [35] Lekan, J. F. and Coney, T. A., "The use of remote sensing to map the areal distribution of cladophora glomerata at a site in lake huron," *Journal of Great Lakes Research* 8(1), 144–152 (1982).
- [36] Wezernak, C. and Lyzenga, D., "Analysis of cladophora distribution in lake ontario using remote sensing," Remote Sensing of Environment 4, 37–48 (1975).
- [37] Sayers, M., Brooks, C., and Shuchman, R., "Mapping and monitoring the extent of submerged aquatic vegetation in the laurentian great lakes with multi-scale satellite remote sensing," in [IAGLR 54th Annual Conference on Great Lakes Research.], 39 (2011).

- [38] Vahtmäe, E. and Kutser, T., "Mapping bottom type and water depth in shallow coastal waters with satellite remote sensing," *Journal of Coastal Research*, 185–189 (2007).
- [39] Vahtmäe, E., Kotta, J., Lõugas, L., and Kutser, T., "Mapping spatial distribution, percent cover and biomass of benthic vegetation in optically complex coastal waters using hyperspectral casi and multispectral sentinel-2 sensors," *International Journal of Applied Earth Observation and Geoinformation* 102, 102444 (2021).
- [40] Kislik, C., Genzoli, L., Lyons, A., and Kelly, M., "Application of uav imagery to detect and quantify submerged filamentous algae and rooted macrophytes in a non-wadeable river," *Remote Sensing* **12**(20) (2020).
- [41] Flynn, K. F. and Chapra, S. C., "Remote sensing of submerged aquatic vegetation in a shallow non-turbid river using an unmanned aerial vehicle," *Remote Sensing* **6**(12), 12815–12836 (2014).
- [42] Eghbali Babadi, F., Boonnoun, P., Nootong, K., Powtongsook, S., Goto, M., and Shotipruk, A., "Identification of carotenoids and chlorophylls from green algae chlorococcum humicola and extraction by liquefied dimethyl ether," *Food and Bioproducts Processing* **123**, 296–303 (2020).
- [43] Mangold, K., Shaw, J. A., and Vollmer, M., "The physics of near-infrared photography," *European Journal of Physics* **34**(6), S51 (2013).
- [44] Logan, R. D., Hamp, S. M., Torrey, M. A., Feijo de Lima, R., Colman, B. P., Valett, H., and Shaw, J. A., "Uav-based hyperspectral imaging for river algae pigment estimation and development of a low-cost multispectral imager," in [SPIE Future Sensing Technologies Proceedings 12327], (2023).
- [45] Venkatesulu, E. and Shaw, J. A., "Measuring the spectral response of a division-of-focal-planepolarization imager using a grating monochromator," *Appl. Opt.* **61**(9), 2364–2370 (2022).
- [46] Pagnutti, M. A., Ryan, R. E., V, G. J. C., Gold, M. J., Harlan, R., Leggett, E., and Pagnutti, J. F., "Laying the foundation to use Raspberry Pi 3 V2 camera module imagery for scientific and engineering purposes," *Journal of Electronic Imaging* 26(1), 013014 (2017).